Advanced Materials

ADVANCED MATERIALS
www.advmat.de

RESEARCH ARTICLE OPEN ACCESS

Giant Orbital Rashba–Edelstein Effect in Crystalline Cu_2O/Cu Heterostructures

San Ko[1] | Jaimin Kang[2,3] | Su Jae Kim[4] | Hanhwi Jang[2] | Do-Kyeong Nam[1] | Minseok Kang[2] | Sunghoon Kim[2] | Yeon Sik Jung[2] | Se-Young Jeong[1,5] | Kab-Jin Kim[1,6] | Byong-Guk Park[2]

[1]Department of Physics, KAIST, Daejeon, Republic of Korea | [2]Department of Materials Science and Engineering, KAIST, Daejeon, Republic of Korea | [3]Department of Electrical and Computer Engineering, Northwestern University, Evanston, Illinois, USA | [4]Crystal Bank Research Institute, Pusan National University, Busan, Republic of Korea | [5]Department of Optics and Mechatronics Engineering, Engineering Research Center For Color-Modulated Extra-Sensory Perception Technology, Pusan National University, Busan, Republic of Korea | [6]Graduate School of Quantum Science and Technology, KAIST, Daejeon, Republic of Korea

Correspondence: Se-Young Jeong (sjeong9@kaist.ac.kr) | Kab-Jin Kim (kabjin@kaist.ac.kr) | Byong-Guk Park (bgpark@kaist.ac.kr)

Received: 29 January 2026 | **Revised:** 30 April 2026 | **Accepted:** 21 May 2026

Keywords: crystalline oxide | orbital current | orbital Rashba–Edelstein effect | orbital torque

ABSTRACT

Orbital current-induced torque (OT) has emerged as a promising alternative to spin–orbit torque owing to the typically larger orbital Hall conductivity. A substantial OT can be generated at metal/oxide interfaces via the orbital Rashba–Edelstein effect (OREE), which has been predominantly reported in surface-oxidized Cu structures. However, the lack of well-defined crystalline and interfacial structures in oxidized Cu has hindered a clear understanding of the underlying mechanism and limited further enhancement of OT. Here, we demonstrate a significantly enhanced OREE in crystalline CuO_x/Cu heterostructures with well-defined interfaces. By employing controlled oxidation of single-crystalline Cu, we fabricate crystalline CuO_x layers with distinct chemical phases and quantify the resulting OT using harmonic Hall measurements. We find that the crystalline Cu_2O/Cu heterostructure exhibits a damping-like OT efficiency approximately seven times larger than that of naturally oxidized Cu, highlighting the crucial role of structural ordering and interface sharpness. Notably, this large OT efficiency, combined with the high electrical conductivity of Cu, yields a spin torque conductivity of 1.9×10^6 $(\hbar/2e)\Omega^{-1}$ m^{-1}, exceeding that of Pt. These results establish crystalline Cu_2O/Cu heterostructures as a promising platform for ultralow-power spin-orbitronic devices.

1 | Introduction

Spin-orbit torque (SOT) offers ultrafast and energy-efficient magnetization switching, making it a promising writing scheme for a wide range of spintronic applications, including magnetoresistive random-access memory and spin logic devices [1, 2]. In SOT-based devices, an in-plane charge current generates a transverse spin current via the spin Hall effect (SHE), which exerts a torque on an adjacent ferromagnet and controls its magnetization direction [3–5]. The charge-to-spin conversion efficiency is commonly characterized by the effective spin Hall angle (θ_{SH}^{eff}). Considerable effort has therefore focused on developing materials with large θ_{SH}^{eff}, including heavy metals with strong spin–orbit coupling (β-Ta [5], Pt [6], β-W [7]), van der Waals materials ($MoTe_2$ [8], WTe_2 [9], $PtTe_2$ [10]), topological insulators ($Bi_xSe_{(1-x)}$) [11, 12], antiferromagnets (Mn_2Au [13], PtMn [14], Mn_3Sn [15]), and altermagnets (RuO_2) [16].

San Ko and Jaimin Kang contributed equally to this work.

However, materials exhibiting large $\theta_{\mathrm{SH}}^{\mathrm{eff}}$ often suffer from low electrical conductivity (σ) [7, 12, 17], leading to increased switching power due to enhanced Joule heating. In this context, a more appropriate figure of merit for evaluating spin current source materials is the spin torque conductivity, which incorporates electrical conductivity and is defined as $\sigma_{\mathrm{ST}} = \xi_{\mathrm{DL}}^{j} \times \sigma$, where ξ_{DL}^{j} is the damping-like torque efficiency, equivalent to $\theta_{\mathrm{SH}}^{\mathrm{eff}}$ in SHE-based systems [18]. Pt exhibits one of the largest reported σ_{ST} values of $(2\sim5) \times 10^5$ $(\hbar/2e)\Omega^{-1}\mathrm{m}^{-1}$ [18, 19], and only a limited number of materials have exceeded this value to date [11, 20]. Therefore, to enable the practical implementation of SOT in spintronic devices, the switching current density must be comparable to or lower than that required for conventional spin-transfer torque switching, necessitating the development of SOT materials with substantially enhanced σ_{ST}.

Recently, orbital torque (OT), arising from orbital angular momentum, has emerged as a promising route for enhancing σ_{ST}, owing to the typically larger orbital Hall conductivity compared to the spin Hall conductivity [21, 22]. OT can be generated via the orbital Hall effect (OHE), in which a charge current induces a transverse orbital current, a flow of orbital angular momentum [23, 24]. Unlike the SHE, the OHE is independent of spin–orbit coupling and can therefore occur in a broad range of materials from 3*d* to 5*d* transition metals [25, 26]. Experimental studies have demonstrated sizable OT in light metals such as Ti, Cr, and Ru when combined with interfacial orbital-to-spin conversion layers [27–29]. In particular, bilayers such as Ru/Pt and Ti/Ta have shown OT efficiencies exceeding those of the conventional SOT structures [28, 29]. However, the orbital diffusion length in typical OHE materials has been reported to be on the order of several to tens of nanometers [29–31], which is generally larger than the spin diffusion length [31, 32]. As a result, OHE-based approaches require relatively thick orbital source layers to achieve maximum OT efficiency, resulting in increased switching currents and higher power consumption.

Another approach to generating OT is the interfacial orbital Rashba–Edelstein effect (OREE), in which orbital angular momentum is induced by an electric field at an interface with broken inversion symmetry [33]. Due to its interfacial origin, the OREE is inherently less sensitive to the thickness of the layer structure than bulk OHE-based mechanisms. To date, the most extensively studied systems for OREE-induced OT have been Cu/oxide heterostructures [34–39]. However, previous studies have primarily relied on naturally oxidized Cu [34–36], reactively sputtered Cu oxides [37, 38], or Cu/oxides (Al_2O_3, SiO_2) [39]. These approaches are likely to create mixed oxide phases or amorphous layers with poorly defined interfaces, as schematically illustrated in Figure 1a. Moreover, such structures inevitably introduce oxygen concentration gradients, leading to spatial variations in drift velocity. These variations can generate additional spin torques via spin-vorticity coupling (SVC) [40, 41], which are difficult to distinguish from genuine OREE-induced OT. Therefore, to unambiguously identify the underlying OREE mechanism and to further enhance OT, it is essential to investigate crystalline CuO_x/Cu heterostructures with sharp and well-defined interfaces, as described in Figure 1b.

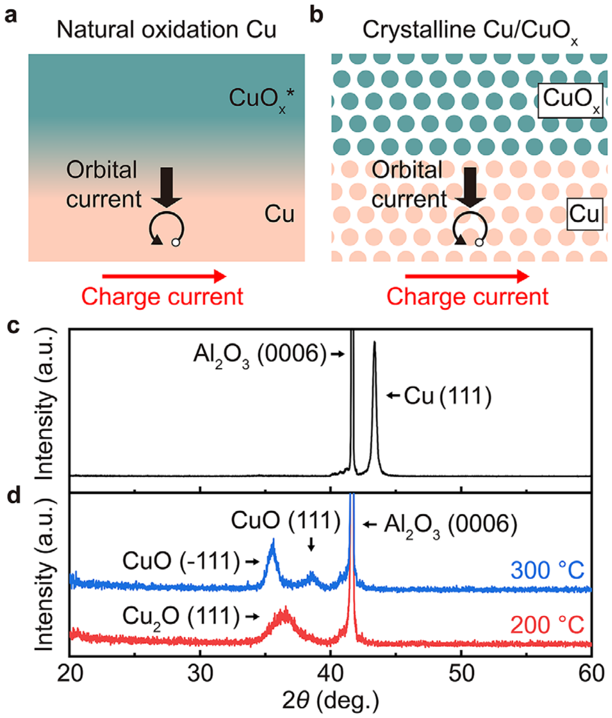

FIGURE 1 | Schematic illustrations of (a) a naturally oxidized Cu surface, which forms a diffuse Cu/CuO_x interface, and (b) a crystalline Cu/CuO_x sample with an atomically sharp and structurally ordered interface. When applying a charge current, a transverse orbital current is generated at the Cu/CuO_x interface via OREE. (c) XRD 2θ scan of the single crystalline Cu (111) film. (d) XRD 2θ scans of the films annealed at 200°C (red), 300°C (blue).

In this work, we investigate the OREE in crystalline CuO_x/Cu heterostructures with well-defined interfaces, realized through controlled oxidation of single-crystalline Cu at elevated temperatures. We observe a significant enhancement of a damping-like OT efficiency in crystalline Cu_2O/Cu/NiFe heterostructures compared to naturally oxidized CuO_x/Cu/NiFe structures. Moreover, combined with the high electrical conductivity of the Cu layer, the spin torque conductivity at the crystalline Cu_2O/Cu interface reaches 1.9×10^6 $(\hbar/2e)\Omega^{-1}$ m^{-1}, approximately four times larger than that of a Pt/NiFe control sample. These results establish a clear correlation between OREE-driven OT and interfacial structural properties and highlight crystalline Cu_2O/Cu heterostructures as a promising route toward low-power orbitronic devices.

2 | Results

To investigate the OREE in crystalline CuO_x/Cu heterostructures, we fabricated crystalline Cu oxide layers using the procedure described below. First, single-crystalline Cu (111) films were grown on Al_2O_3 (0001) substrates using atomic sputtering epitaxy [42], as confirmed by X-ray diffraction (XRD) [Figure 1c]. The Cu (111) films were subsequently oxidized under a mixed Ar (83%)/O_2 (17%) atmosphere at elevated temperatures of 200°C and 300°C (see Methods). Owing to the grain-boundary-free and atomically flat Cu layers along with well-controlled oxidation conditions, this approach enables the growth of crystalline CuO_x phases [43].

Figure 1d shows the XRD spectra of the oxidized films. For the sample oxidized at 200°C, a single diffraction peak corresponding to the Cu_2O (111) plane is observed, whereas the sample oxidized at 300°C exhibits two diffraction peaks corresponding to CuO (−111) and (111) planes. These results indicate that the two samples possess distinct crystalline phases, and that oxidation at higher temperature results in a higher oxidation state, as expected. Hereafter, the sample oxidized at 200°C (300°C) is referred to as the Cu_2O (CuO) sample. Finally, a 10-nm-thick Cu layer was deposited on the oxidized films to form CuO_x/Cu heterostructures.

To examine the crystallinity and interfacial quality, we performed cross-sectional scanning transmission electron microscopy (STEM) measurements on the fabricated CuO_x/Cu samples. Note that a NiFe layer (4 nm), a widely used ferromagnetic layer in studies of the OREE, was deposited on top of the CuO_x/Cu heterostructure for spin torque characterization. This enables direct and quantitative comparison with previously reported results on naturally oxidized Cu and spin Hall-based Pt/NiFe control samples, as will be discussed later. Figure 2a shows a STEM image of the Cu_2O sample (oxidized at 200°C), in which a clear contrast difference between the Cu and CuO_x layers is observed. A magnified STEM image (Figure 2b) reveals well-ordered atomic lattices in both the Cu and CuO_x layers, indicating the formation of crystalline phases. Electron diffraction patterns acquired from the designated area of each layer exhibit sharp diffraction spots, demonstrating their single-crystalline nature. From the (111) diffraction spot aligned along the out-of-plane direction, the interplanar spacing of the CuO_x (111) plane is extracted to be approximately 0.250 nm, which is consistent with the literature value for Cu_2O, $d_{Cu_2O(111)} = 0.246$ nm (ICDD PDF no 01-071-3645). Similarly, the interplanar spacing of the Cu (111) plane is determined to be approximately 0.209 nm, in agreement with the literature value of $d_{Cu(111)} = 0.209$ nm (ICDD PDF no 01-070-3039). These results confirm the successful growth of a crystalline Cu_2O (111)/Cu (111) heterostructure with a sharp and well-defined interface.

Figure 2c,d present the STEM results for the CuO sample (oxidized at 300°C), revealing a well-defined CuO/Cu interface, clearly resolved atomic lattices within both layers, and sharp diffraction spots, which are qualitatively similar to those observed in the Cu_2O sample. Electron diffraction patterns, together with XRD results, confirm the formation of a CuO (−111)/Cu (111) heterostructure. The interplanar spacings extracted from the out-of-plane diffraction spots are approximately 0.255 nm for CuO and 0.205 nm for Cu, which are in good agreement with the literature values of $d_{CuO(-111)} = 0.252$ nm (ICDD PDF no 01-080-0076) and $d_{Cu(111)} = 0.209$ nm, respectively. We also observed a thin interfacial layer, highlighted by the green box in Figure 2d, whose lattice spacing differs from that of the CuO layer, suggesting the presence of additional CuO_x phases at the interface (Figure S1). The potential impact of these interfacial CuO_x phases on the OT will be discussed later.

For comparison, we also fabricated a naturally oxidized Cu sample (denoted as CuO_x* hereafter), which was prepared by depositing a metallic Cu layer followed by exposure to ambient atmosphere for 72 h. Due to this oxidation procedure, the layer sequence in the CuO_x* structure–in which a ferromagnetic NiFe is located beneath the Cu layer is inverted relative to that of the crystalline CuO_x/Cu heterostructures described above. Figure 2e shows a STEM image of the CuO_x* sample, which does not exhibit a clear contrast difference within the layer, indicating a highly diffuse interfacial region between the metallic Cu and CuO_x* layers. A magnified STEM image (Figure 2f) reveals the absence of well-ordered atomic lattices, while the electron diffraction pattern displays ring-like features in both the Cu and CuO_x* regions, characteristic of an amorphous structure. Taken together, these results demonstrate that the naturally oxidized Cu heterostructure is predominantly amorphous and lacks a distinct interface, in sharp contrast to the crystalline CuO_x/Cu heterostructures. We note that the NiFe layer grown on crystalline CuO_x/Cu heterostructures does not exhibit a well-defined crystalline phase (Figures S2 and S3).

To investigate the OT exerted on the ferromagnetic NiFe layer induced by OREE at the CuO_x/Cu interface, we performed in-plane harmonic Hall measurements on the Cu_2O, CuO, and CuO_x* samples. Figure 3a illustrates the measurement configuration using a Hall-bar device with a width of 10 µm, in which harmonic Hall resistances were measured under an ac current and an external magnetic field (B_{ext}). Figure 3b,c show representative first harmonic resistances ($R_{xy1\omega}$) of the Cu_2O sample as functions of the out-of-plane magnetic field (B_z) and the in-plane field angle (φ), respectively. From these measurements, we extracted the anomalous Hall resistance (R_{AHE}) and planar Hall resistance (R_{PHE}). Figure 3d presents a representative second harmonic Hall resistance ($R_{xy}^{2\omega}$) as a function of φ under different external magnetic fields (B_{ext}) ranging from 0.15 to 1 T, measured at a current density $J_{Cu} = 1.28\times10^7\ Acm^{-2}$. The angular dependence of $R_{xy}^{2\omega}(\varphi)$ is expressed as [44, 45]

$$R_{xy}^{2\omega}(\varphi) = \left(R_{AHE}\frac{B_{DLT}}{B_{eff}} + R_{\nabla T}\right)\cos\varphi + 2R_{PHE}\frac{B_{FLT}+B_{Oe}}{B_{ext}}\left(2\cos^3\varphi - \cos\varphi\right) \qquad (1)$$

Here, B_{DLT} (B_{FLT}) is the damping-like (field-like) torque-induced effective field, $R_{\nabla T}$ is the thermal contributions, and B_{Oe} is the current-induced Oersted field. B_{eff} is the effective magnetic field, defined as $B_{eff} = B_{ext} + B_{dem} - B_{ani}$, where B_{dem} and B_{ani} are the demagnetizing field and the anisotropy field of ferromagnet, respectively, and the value of $B_{dem} - B_{ani}$ was obtained from Figure 3b. From the $R_{xy}^{2\omega}(\varphi)$ curves, we separated the $\cos\varphi$ and $2\cos^3\varphi - \cos\varphi$ components, denoted as $R_{xy,\ \cos\varphi}^{2\omega}$ and $R_{xy,\ 2\cos^3\varphi-\cos\varphi}^{2\omega}$, respectively, and then plotted a $R_{xy,\ \cos\varphi}^{2\omega}/R_{AHE}$ as a function of $1/B_{eff}$ and $R_{xy,\ 2\cos^3\varphi-\cos\varphi}^{2\omega}/R_{PHE}$ against $1/B_{ext}$ curve in Figure 3e,f, respectively. From the slopes of linear fits, the OT-induced effective fields for the Cu_2O sample were extracted to be $B_{DLT} = 1.98 \pm 0.42$ mT and $B_{FLT} + B_{Oe} = -0.20 \pm 0.01$ mT.

The same measurements were repeated for the CuO and CuO_x* samples. Figure 3g,j show the corresponding $R_{xy}^{2\omega}(\varphi)$ curves measured at the same current density ($J_{Cu} = 1.28 \times 10^7\ Acm^{-2}$). Note that the sign reversal observed for the CuO_x* sample is due to the inverted stacking order of the heterostructure.

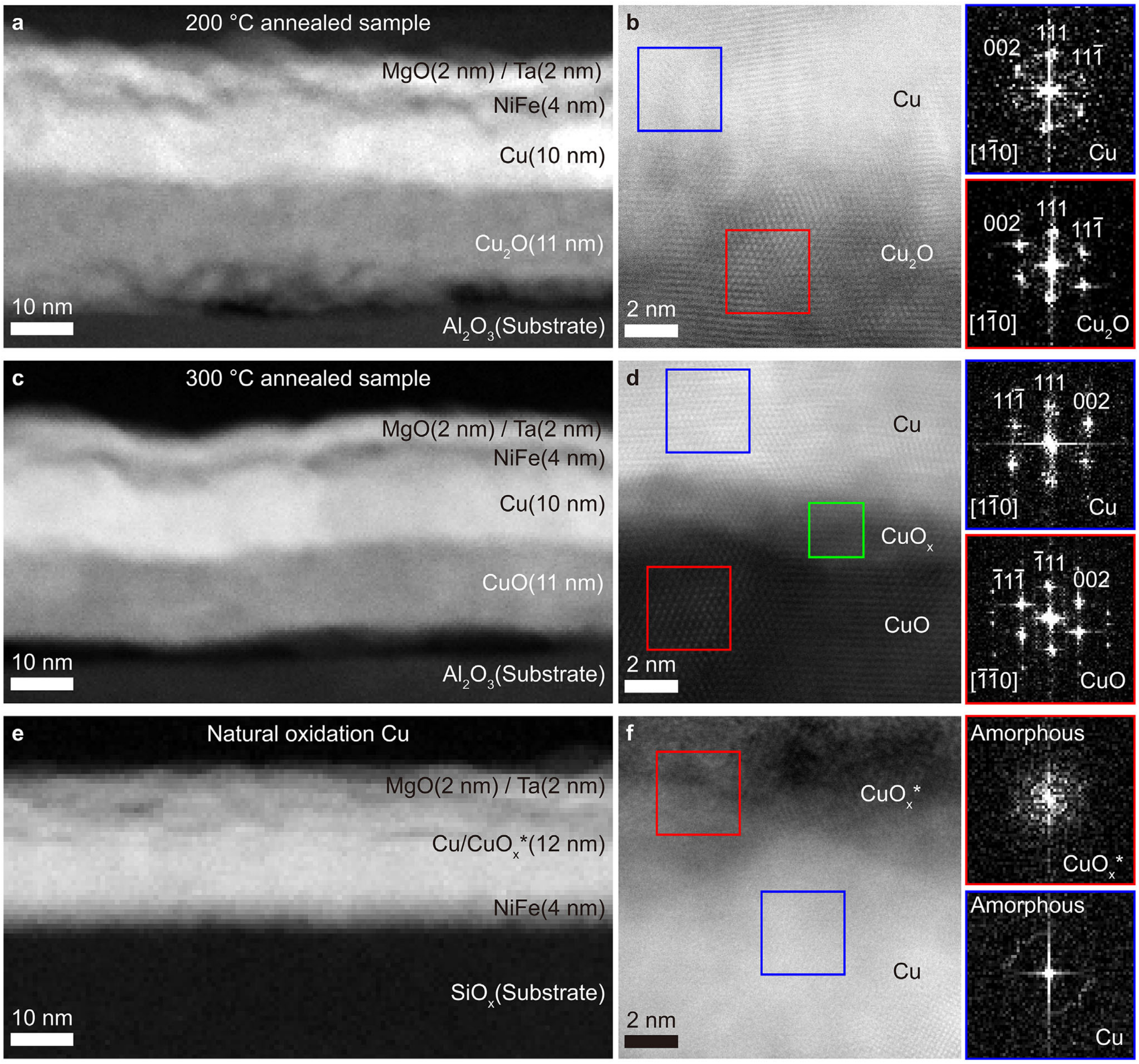

FIGURE 2 | (a) A cross-sectional STEM image of the 200°C annealed sample (Cu_2O sample). (b) A magnified STEM image and the corresponding diffraction patterns extracted from the regions marked by the blue box (Cu) and the red box (Cu_2O). (c) A cross-sectional STEM image of the 300°C annealed sample (CuO sample). (d) A magnified STEM image and the corresponding diffraction patterns extracted from the regions marked by the blue box (Cu) and the red box (CuO), while the green box indicates a mixed CuO_x phase region. (e) A cross-sectional STEM image of the naturally oxidized Cu sample (CuO_x* sample). (f) Magnified STEM image and the corresponding diffraction patterns extracted from the regions marked by the blue box (Cu) and the red box (CuO_x*).

Using the same analysis procedure, the extracted B_{DLT} values are 0.94 ± 0.42 mT for the CuO sample (Figure 3h) and −0.20 ± 0.14 mT for the CuO_x* sample (Figure 3i), while $B_{\mathrm{FLT}} + B_{\mathrm{Oe}}$ values are −0.20 ± 0.01 mT for the CuO sample (Figure 3k), and 0.14 ± 0.01 mT for the CuO_x* sample (Figure 3l). These results demonstrate that B_{DLT} strongly depends on the oxidation state of the CuO_x layer, exhibiting the largest value for the Cu_2O sample and the smallest for the CuO_x* sample. In contrast, $B_{\mathrm{FLT}} + B_{\mathrm{Oe}}$ remains small and nearly independent of the oxidation state, indicating this contribution is dominated by B_{Oe}. Note that the observed torques of the CuO_x* sample are comparable to those reported for similar structures in previous studies [46, 47] and show only a slight variation upon inversion of the stacking order (Figure S4). Additionally, the intercepts in $R^{2\omega}_{xy,\,\cos\varphi}/R_{\mathrm{AHE}}$ versus $1/B_{\mathrm{eff}}$ curves reflect thermal contributions ($R_{\nabla T}$) in each sample. The smaller intercepts in Cu_2O and CuO samples suggest that the thermal contributions are suppressed in crystalline Cu oxide samples, likely due to differences in thermal transport arising from variations in the substrate and layer structure.

We further examined the possible contribution of SVC by measuring electron energy loss spectroscopy (EELS) depth profiles and the Cu thickness dependence of ξ^{j}_{DL}. The former shows no

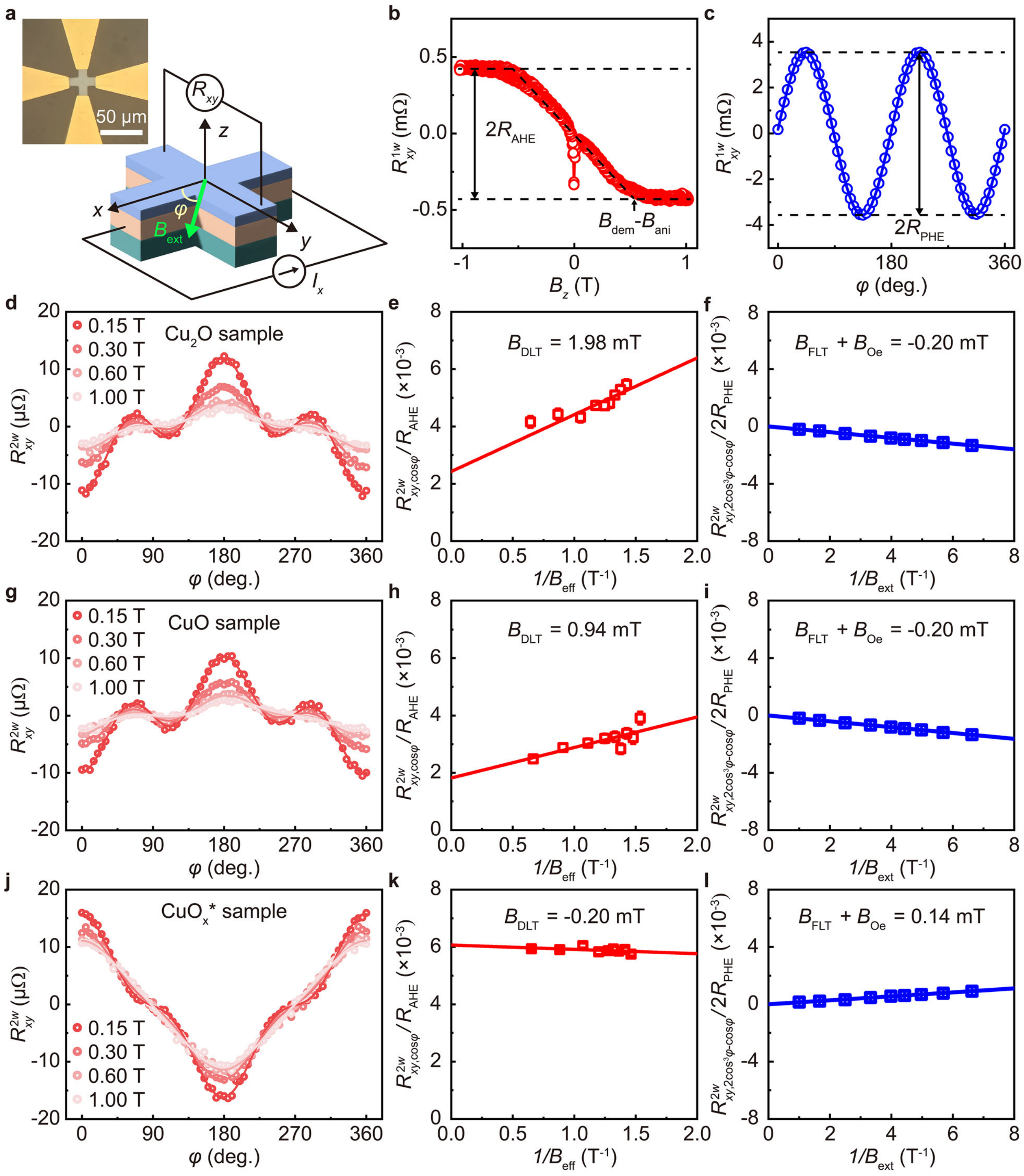

FIGURE 3 | (a) Schematic illustrations of the Hall-bar device and harmonic Hall measurement geometry. (b,c) R_{xy}^{1w} of the Cu$_2$O sample as a function of (b) external magnetic field B_z and (c) in-plane field angle φ. (d) Azimuthal angle φ dependent R_{xy}^{2w} for the Cu$_2$O sample under various in-plane magnetic fields at a current density $J_{Cu} = 1.28 \times 10^7\ Acm^{-2}$. (e) $R_{xy,\ \cos\varphi}^{2w}/R_{AHE}$ as a function of $1/B_{eff}$, where the slope of the linear fit provides the B_{DLT}, (f) $R_{xy,\ 2\cos^3\varphi-\cos\varphi}^{2w}/R_{PHE}$ against $1/B_{ext}$, where the slope of the linear fit provides the $B_{FLT} + B_{Oe}$. The same measurements and analyses for the (g–i) CuO sample and the (j–l) CuO$_x$* sample.

pronounced oxygen gradient (Figures S5 and S6), and the latter exhibits a non-monotonic thickness dependence of ξ_{DL}^{j} (Figures S7–S9), in contrast to the expected increase in SVC-induced torque with Cu conductivity [41]. These results suggest that SVC is unlikely to be the primary origin of the observed torque.

We next quantified the damping-like torque efficiency (ξ_{DL}^{j}), which is expressed as $\xi_{DL}^{j} = (2e/\hbar)(M_S t_{NiFe} B_{DLT}/J_{Cu})$, where, M_S and t_{NiFe} are the saturation magnetization and thickness of the NiFe layer, respectively, and J_{Cu} is the current density flowing in the Cu layer. To determine ξ_{DL}^{j}, we performed harmonic

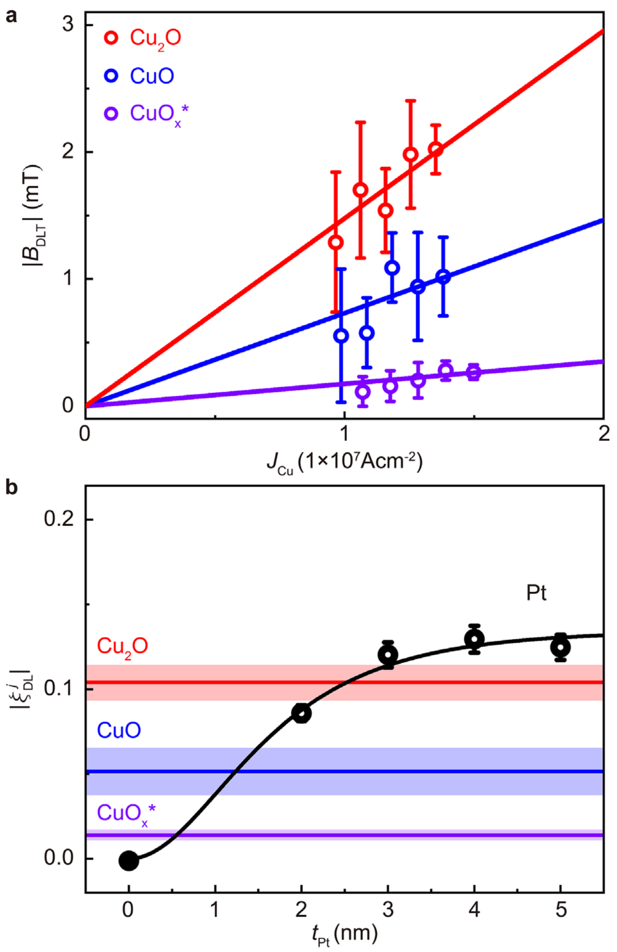

FIGURE 4 | (a) Magnitude of B_{DLT} as a function of the current density (J_{Cu}) flowing through the Cu layer for the Cu_2O/Cu/NiFe, CuO/Cu/NiFe, and NiFe/CuO_x* samples. (b) Extracted ξ_{DL}^{j} of the Cu_2O, CuO, and CuO_x* samples compared with the Pt (t_{Pt})/NiFe reference samples. The blurred regions represent the corresponding error bars.

Hall measurements for the Cu_2O, CuO, CuO_x* samples under various current densities (Figures S10–S15). Figure 4a presents the extracted B_{DLT} values as a function of J_{Cu} for the three samples. From the slopes of the linear fits, we obtained ξ_{DL}^{j} values of 0.102 ± 0.011, 0.052 ± 0.014, and 0.014 ± 0.003 for the Cu_2O, CuO, and CuO_x* sample, respectively. Consistent with the B_{DLT} behavior, the Cu_2O sample exhibits the largest ξ_{DL}^{j}, followed by the CuO and CuO_x* samples. We also obtained consistent ξ_{DL}^{j} values from spin-torque ferromagnetic resonance measurements, further corroborating the enhancement of ξ_{DL}^{j} in crystalline Cu oxide systems (Figures S16 and S17). Notably, the ξ_{DL}^{j} of the crystalline Cu_2O sample is nearly an order of magnitude larger than that of the naturally oxidized CuO_x* sample. This pronounced enhancement of ξ_{DL}^{j} is attributed to the strengthened OREE at the sharp and well-defined crystalline CuO_x/Cu interface. While OREE in Cu_2O-based structures has been previously reported [48, 49], its magnitude remains relatively limited, likely due to reduced crystallinity associated natural oxidation. Note that although the CuO sample is also crystalline, its ξ_{DL}^{j} value is smaller than that of the Cu_2O sample. This may be attributed to excessive oxidation and/or the presence of mixed or disordered CuO_x phases at the interface, which can suppress the OREE [38]. This interpretation is supported by the interfacial lattice spacing observed in STEM that does not correspond to any known CuO_x phases (Figure S1). Taken together, these results further corroborate that both the oxidation states and interfacial quality play a critical role in determining the efficiency of OREE-driven OT.

To benchmark the ξ_{DL}^{j} originating from the OREE at the CuO_x/Cu interface against a conventional SOT material, we measured ξ_{DL}^{j} in Pt (t_{Pt} nm)/NiFe (4 nm) structures (t_{Pt} = 0–5 nm) (Figures S18–S21). Figure 4b shows ξ_{DL}^{j} as a function of t_{Pt}. No detectable ξ_{DL}^{j} was observed in the single NiFe sample ($t_{Pt} = 0$), indicating negligible self-induced torque in our system (Figure S22). From the Pt thickness dependence, we extracted a $\xi_{DL,Pt}^{j}$ of 0.134 and a spin diffusion length λ_s of 1.16 nm, which are consistent with previously reported values [50–52]. Remarkably, our crystalline Cu_2O/Cu sample exhibits a ξ_{DL}^{j} comparable to that of Pt, highlighting the effectiveness of the OREE at the crystalline Cu_2O/Cu heterostructure.

Lastly, we discuss a key advantage of the crystalline Cu_2O/Cu heterostructure in terms of the spin torque conductivity ($\sigma_{ST} = \xi_{DL}^{j} \times \sigma$). The conductivity ($\sigma$) of Cu was extracted from thickness-dependent resistance measurements using the Fuchs-Sondheimer (FS) model, which accounts for size-dependent scattering effects in thin film (Figures S23 and S24). Although the ξ_{DL}^{j} of our crystalline Cu_2O/Cu sample is a slightly lower than that of Pt, the resulting σ_{ST} reaches $1.90 \times 10^6 (\hbar/2e)\Omega^{-1}m^{-1}$, which is approximately four times larger than that of Pt ($\sigma_{ST} = 5.10 \times 10^5 (\hbar/2e)\Omega^{-1}m^{-1}$). This enhancement originates from the substantially higher electrical conductivity of crystalline Cu compared to Pt ($\sigma_{Cu_2O/Cu} = 1.86 \times 10^7$ S/m, $\sigma_{Pt} = 0.38 \times 10^7$ S/m). We further compare the σ_{ST} and σ values of our samples with those in previous studies, including naturally oxidized Cu [46, 53, 54], OHE-based materials [27, 28], SHE-based materials [5, 7, 55], van der Waals materials [8, 10, 56], topological insulators [12], and altermagnets [16], as summarized in Figure 5. Among all systems considered, the crystalline Cu_2O/Cu heterostructure exhibits the highest σ_{ST}, highlighting its strong potential as a materials platform for ultralow-power spin-orbitronic devices.

3 | Conclusion

We have demonstrated a strongly enhanced OREE in crystalline CuO_x/Cu heterostructures. By systematically investigating crystalline Cu_2O/Cu and CuO/Cu structures in comparison to naturally oxidized CuO_x*/Cu, we establish that crystallinity and interface quality play critical roles in determining the OREE and the resulting OT. The pronounced enhancement observed in the crystalline Cu_2O/Cu heterostructure suggests that structural ordering at the interface can give rise to a uniform interfacial electric field and enhanced orbital hybridization, thereby facilitating well-defined orbital angular momentum textures that strengthen the OREE. Furthermore, the enhanced OREE, combined with the intrinsically high electrical conductivity of crystalline Cu, results in an exceptionally large spin torque conductivity that surpasses previously reported values. These findings not only provide clear physical insight into the structural factors governing

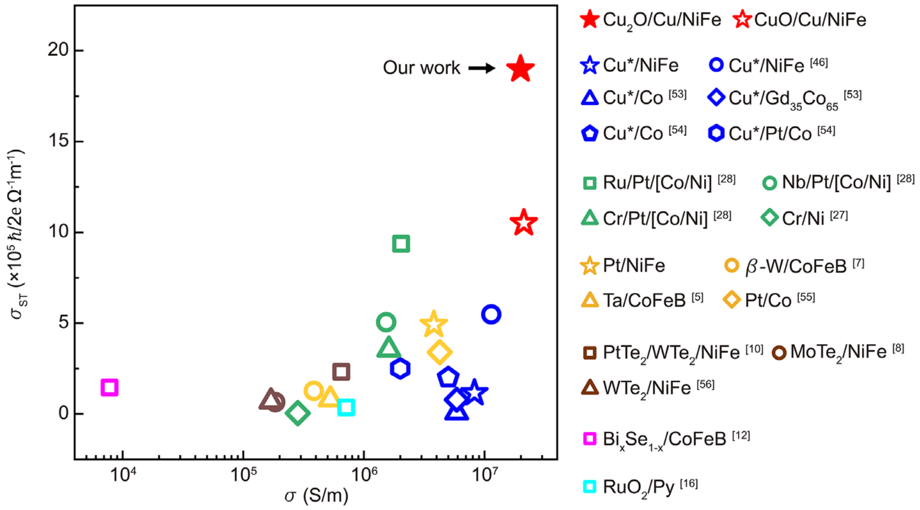

FIGURE 5 | Comparison of σ_{ST} and σ values across different material systems. The data include crystalline CuO$_x$/Cu systems (red), naturally oxidized Cu-based systems (blue), orbital Hall sources (green), spin Hall sources (yellow), van der Waals materials (brown), topological insulators (magenta), and altermagnets (cyan) reported in the literature. The star symbols indicate data points obtained in this work.

OREE-driven OT, but also demonstrate the crystalline Cu$_2$O/Cu heterostructure as a viable materials platform for achieving efficient current-induced switching without relying on heavy elements, with strong potential for ultralow-power spin-orbitronic devices.

4 | Experimental Section/Methods

4.1 | Sample Preparation

To fabricate high-quality crystalline Cu oxide, we first deposited single-crystalline Cu on a 430 µm-thick Al$_2$O$_3$ (0001) substrate at 170°C by RF sputtering using atomic sputtering epitaxy (ASE) [42]. The base pressure and working pressure under Ar gas were 2.0×10^{-7} and 5.4×10^{-3} Torr, respectively. ASE incorporates several key modifications compared to conventional sputtering systems, including the use of a bulk single-crystal Cu target, a single-crystal copper wiring network, and mechanical noise reduction systems [43]. These features suppress the formation of grain boundary and minimize the density of twin boundaries by reducing the number of nucleation sites and enabling the nucleated islands to grow into larger crystalline domains. The single-crystal Cu films were then annealed at two different temperatures: 200°C for 120 min and 300°C for 30 min, under a mixed-gas atmosphere of Ar (83%):O$_2$ (17%) [43]. Through the annealing process, the single-crystal Cu films were fully oxidized into crystalline Cu$_2$O film (200 °C) and CuO film (300 °C). Subsequently, Cu (10 nm)/NiFe (4 nm)/MgO (2 nm)/Ta (2 nm) was deposited on the crystalline CuO$_x$ films to form CuO$_x$/Cu heterostructures. For the naturally oxidized Cu sample, NiFe (4 nm)/Cu (10 nm) was first deposited on Si/SiO$_2$ (200 nm) substrate. After exposing the film to the ambient atmosphere for 72 h, MgO (2 nm)/Ta (2 nm) capping layers were deposited to prevent further oxidation. The Pt (t_{Pt} nm)/NiFe (4 nm)/MgO (2 nm)/Ta (2 nm) films were deposited on Si/SiO$_2$ (200 nm) substrates in a single deposition process. The MgO layers were deposited by RF magnetron sputtering, while the other layers were deposited by DC magnetron sputtering under a base pressure of 7×10^{-7} Torr and a working pressure under Ar gas of 3×10^{-3} Torr. Finally, the films were patterned into Hall-bar structures with dimensions of 10 µm in width and 30 µm in length using photolithography and Ar ion milling. Electrical contact pads consisting of 5 nm Ti and 100 nm Au were subsequently fabricated using a lift-off process.

4.2 | Structural Characterization

Thin lamellae samples for the scanning transmission electron microscope (STEM) observation were prepared using a focused ion beam. A standard lift-out technique with ion-beam milling was performed to prepare electron-transparent STEM samples.

4.3 | Electrical Measurements

In-plane harmonic Hall measurement with ac current (313 Hz) was performed to evaluate the effective field of orbital torque. Both $R_{xy}^{1\omega}$ and $R_{xy}^{2\omega}$ were simultaneously detected using two lock-in amplifiers while varying the azimuthal angle (φ) under a constant external field B_{ext} at room temperature using the Hall-bar-patterned devices with widths of 10 µm and lengths of 30 µm.

Acknowledgements

This work was supported by the National Research Foundation (NRF) of Korea (RS-2023-00261042, RS-2024-00410027, RS-2023-00275259, RS-2023-00256050, 2021R1A5A1032937, and RS-2024-00455226).

Conflicts of Interest

The authors declare no conflicts of interest.

Data Availability Statement

The data that support the findings of this study are available from the corresponding author upon reasonable request.

References

1. A. Manchon, J. Zelezný, I. M. Miron, et al., “Current-Induced Spin-Orbit Torques in Ferromagnetic and Antiferromagnetic Systems,” *Reviews of Modern Physics* 91 (2019): 035004, https://doi.org/10.1103/RevModPhys.91.035004.

2. I. Mihai Miron, G. Gaudin, S. Auffret, et al., “Current-Driven Spin Torque Induced by the Rashba Effect in a Ferromagnetic Metal Layer,” *Nature Materials* 9 (2010): 230–234, https://doi.org/10.1038/nmat2613.

3. I. M. Miron, K. Garello, G. Gaudin, et al., “Perpendicular Switching of a Single Ferromagnetic Layer Induced by In-Plane Current Injection,” *Nature* 476 (2011): 189–193, https://doi.org/10.1038/nature10309.

4. J. Ryu, S. Lee, K. J. Lee, and B. G. Park, “Current-Induced Spin–Orbit Torques for Spintronic Applications,” *Advanced Materials* 32 (2020): 1907148, https://doi.org/10.1002/adma.201907148.

5. L. Liu, C.-F. Pai, Y. Li, H. W. Tseng, D. C. Ralph, and R. A. Buhrman, “Spin-Torque Switching With the Giant Spin Hall Effect of Tantalum,” *Science* 336 (2012): 555–558, https://doi.org/10.1126/science.1218197.

6. L. Liu, T. Moriyama, D. C. Ralph, and R. A. Buhrman, “Spin-Torque Ferromagnetic Resonance Induced by the Spin Hall Effect,” *Physical Review Letters* 106 (2011): 036601, https://doi.org/10.1103/PhysRevLett.106.036601.

7. C.-F. Pai, L. Liu, Y. Li, H. W. Tseng, D. C. Ralph, and R. A. Buhrman, “Spin Transfer Torque Devices Utilizing the Giant Spin Hall Effect of Tungsten,” *Applied Physics Letters* 101 (2012): 122404, https://doi.org/10.1063/1.4753947.

8. S. Liang, S. Shi, C.-H. Hsu, et al., “Spin-Orbit Torque Magnetization Switching in MoTe$_2$/Permalloy Heterostructures,” *Advanced Materials* 32 (2020): 2002799, https://doi.org/10.1002/adma.202002799.

9. D. MacNeill, G. M. Stiehl, M. H. D. Guimaraes, R. A. Buhrman, J. Park, and D. C. Ralph, “Control of Spin–Orbit Torques Through Crystal Symmetry in WTe$_2$/Ferromagnet Bilayers,” *Nature Physics* 13 (2016): 300–305, https://doi.org/10.1038/nphys3933.

10. F. Wang, G. Shi, K.-W. Kim, et al., “Field-free Switching of Perpendicular Magnetization by Two-Dimensional PtTe$_2$/WTe$_2$ van der Waals Heterostructures With High Spin Hall Conductivity,” *Nature Materials* 23 (2024): 768–774, https://doi.org/10.1038/s41563-023-01774-z.

11. N. H. D. Khang, Y. Ueda, and P. N. Hai, “A Conductive Topological Insulator With Large Spin Hall Effect for Ultralow Power Spin–Orbit Torque Switching,” *Nature Materials* 17 (2018): 808–813, https://doi.org/10.1038/s41563-018-0137-y.

12. M. DC, R. Grassi, J.-Y. Chen, et al., “Room-Temperature High Spin–Orbit Torque Due to Quantum Confinement in Sputtered Bi$_x$Se$_{(1-x)}$ Films,” *Nature Materials* 17 (2018): 800–807, https://doi.org/10.1038/s41563-018-0136-z.

13. X. Chen, S. Shi, G. Shi, et al., “Observation of the Antiferromagnetic Spin Hall Effect,” *Nature Materials* 20 (2021): 800–804, https://doi.org/10.1038/s41563-021-00946-z.

14. W. Zhang, M. B. Jungfleisch, W. Jiang, et al., “Spin Hall Effects in Metallic Antiferromagnets,” *Physical Review Letters* 113 (2014): 196602, https://doi.org/10.1103/PhysRevLett.113.196602.

15. K. Kondou, H. Chen, T. Tomita, et al., “Giant Field-Like Torque by the Out-Of-Plane Magnetic Spin Hall Effect in a Topological Antiferromagnet,” *Nature Communications* 12 (2021): 6491, https://doi.org/10.1038/s41467-021-26453-y.

16. A. Bose, N. J. Schreiber, R. Jain, et al., “Tilted Spin Current Generated by the Collinear Antiferromagnet Ruthenium Dioxide,” *Nature Electronics* 5 (2022): 267–274, https://doi.org/10.1038/s41928-022-00744-8.

17. H. Wu, P. Zhang, P. Deng, et al., “Room-Temperature Spin-orbit Torque From Topological Surface States,” *Physical Review Letters* 123 (2019): 207205, https://doi.org/10.1103/PhysRevLett.123.207205.

18. M. H. Nguyen, D. C. Ralph, and R. A. Buhrman, “Spin Torque Study of the Spin Hall Conductivity and Spin Diffusion Length in Platinum Thin Films With Varying Resistivity,” *Physical Review Letters* 116 (2016): 126601, https://doi.org/10.1103/PhysRevLett.116.126601.

19. E. Sagasta, Y. Omori, M. Isasa, et al., “Tuning the Spin Hall Effect of Pt From the Moderately Dirty to the Superclean Regime,” *Physical Review B* 94, no. R (2016): 060412, https://doi.org/10.1103/PhysRevB.94.060412.

20. L. Zhu, D. C. Ralph, and R. A. Buhrman, “Highly Efficient Spin-current Generation by the Spin Hall Effect in Au$_{1-x}$Pt$_x$,” *Physical Review Applied* 10 (2018): 031001, https://doi.org/10.1103/PhysRevApplied.10.031001.

21. T. Tanaka, H. Kontani, M. Naito, et al., “Intrinsic Spin Hall Effect and Orbital Hall Effect in 4*d* and 5*d* Transition Metals,” *Physical Review B* 77 (2008): 165117, https://doi.org/10.1103/PhysRevB.77.165117.

22. L. Salemi and P. M. Oppeneer, “First-Principles Theory of Intrinsic Spin and Orbital Hall and Nernst Effects in Metallic Monoatomic Crystals,” *Physical Review Materials* 6 (2022): 095001, https://doi.org/10.1103/PhysRevMaterials.6.095001.

23. D. Go and H.-W. Lee, “Orbital Torque: Torque Generation by Orbital Current Injection,” *Physical Review Research* 2 (2020): 013177, https://doi.org/10.1103/PhysRevResearch.2.013177.

24. D. Go, D. Jo, C. Kim, and H. W. Lee, “Intrinsic Spin and Orbital Hall Effects From Orbital Texture,” *Physical Review Letters* 121 (2018): 086602, https://doi.org/10.1103/PhysRevLett.121.086602.

25. D. Lee, D. Go, H.-J. Park, et al., “Orbital Torque in Magnetic Bilayers,” *Nature Communications* 12 (2021): 6710, https://doi.org/10.1038/s41467-021-26650-9.

26. Y.-G. Choi, D. Jo, K.-H. Ko, et al., “Observation of the Orbital Hall Effect in a Light Metal Ti,” *Nature* 619 (2023): 52–56, https://doi.org/10.1038/s41586-023-06101-9.

27. S. Lee, M.-G. Kang, D. Go, et al., “Efficient Conversion of Orbital Hall Current to Spin Current for Spin-Orbit Torque Switching,” *Communications Physics* 4 (2021): 234, https://doi.org/10.1038/s42005-021-00737-7.

28. R. Gupta, C. Bouard, F. Kammerbauer, et al., “Harnessing Orbital Hall Effect in Spin-Orbit Torque MRAM,” *Nature Communications* 16 (2025): 130, https://doi.org/10.1038/s41467-024-55437-x.

29. S. Shin, D. Han, S. Lee, and B. G. Park, “Enhanced Magnetization Switching Efficiency via Orbital-Current-Induced Torque in Ti/Ta (Pt)/CoFeB/MgO Structures,” *Advanced Functional Materials* 35 (2025): 2425932, https://doi.org/10.1002/adfm.202425932.

30. A. Bose, F. Kammerbauer, R. Gupta, et al., “Detection of Long-range Orbital-Hall Torques,” *Physical Review B* 107 (2023): 134423, https://doi.org/10.1103/PhysRevB.107.134423.

31. H. Hayashi, D. Jo, D. Go, et al., “Observation of Long-range Orbital Transport and Giant Orbital Torque,” *Communications Physics* 6 (2023): 32, https://doi.org/10.1038/s42005-023-01139-7.

32. T. S. Seifert, D. Go, H. Hayashi, et al., “Time-Domain Observation of Ballistic Orbital-Angular-Momentum Currents With Giant Relaxation Length in Tungsten,” *Nature Nanotechnology* 18 (2023): 1132–1138, https://doi.org/10.1038/s41565-023-01470-8.

33. D. Go, D. Jo, T. Gao, et al., “Orbital Rashba Effect in a Surface-Oxidized Cu Film,” *Physical Review B* 103 (2021): L121113, https://doi.org/10.1103/PhysRevB.103.L121113.

34. H. An, Y. Kageyama, Y. Kanno, N. Enishi, and K. Ando, “Spin–Torque Generator Engineered by Natural Oxidation of Cu,” *Nature Communications* 7 (2016): 13069, https://doi.org/10.1038/ncomms13069.

35. S. Ding, Z. Liang, D. Go, et al., “Observation of the Orbital Rashba-Edelstein Magnetoresistance,” *Physical Review Letters* 128 (2022): 067201, https://doi.org/10.1103/PhysRevLett.128.067201.

36. W. Gao, L. Liao, H. Isshiki, et al., “Nonlocal Electrical Detection of Reciprocal Orbital Edelstein Effect,” *Nature Communications* 16 (2025): 6380, https://doi.org/10.1038/s41467-025-61602-7.

37. Y. Kageyama, Y. Tazaki, H. An, et al., "Spin-Orbit Torque Manipulated by Fine-Tuning of Oxygen-Induced Orbital Hybridization," *Science Advances* 5 (2019): aax4278, https://doi.org/10.1126/sciadv.aax4278.

38. C. J. Li and C. F. Pai, "Oxidation-Tuned CuO_x for Spin–Orbit Torque Efficiency Enhancement," *ACS Applied Materials & Interfaces* 17 (2025): 60845–60851, https://doi.org/10.1021/acsami.5c15854.

39. J. Kim, J. Uzuhashi, M. Horio, et al., "Oxide Layer Dependent Orbital Torque Efficiency in Ferromagnet/Cu/Oxide Heterostructures," *Physical Review Materials* 7 (2023): L111401, https://doi.org/10.1103/PhysRevMaterials.7.L111401.

40. G. Okano, M. Matsuo, Y. Ohnuma, S. Maekawa, and Y. Nozaki, "Nonreciprocal Spin Current Generation in Surface-Oxidized Copper Films," *Physical Review Letters* 122 (2019): 217701, https://doi.org/10.1103/PhysRevLett.122.217701.

41. L. Yi, T. Yang, C. Tan, et al., "Large Orbital Torque From Interfacial Spin-Vorticity Coupling in PtCo/Cu Heterostructures," *Physical Review Letters* 135 (2025): 156702, https://doi.org/10.1103/qgdy-k39l.

42. S. J. Kim, Y. I. Kim, B. Lamichhane, et al., "Flat-Surface-Assisted and Self-Regulated Oxidation Resistance of Cu(111)," *Nature* 603 (2022): 434–438, https://doi.org/10.1038/s41586-021-04375-5.

43. S. J. Kim, S. Kim, J. Lee, et al., "Color of Copper/Copper Oxide," *Advanced Materials* 33 (2021): 2007345, https://doi.org/10.1002/adma.202007345.

44. M. Hayashi, J. Kim, M. Yamanouchi, and H. Ohno, "Quantitative Characterization of the Spin-Orbit Torque Using Harmonic Hall Voltage Measurements," *Physical Review B* 89 (2014): 144425, https://doi.org/10.1103/PhysRevB.89.144425.

45. C. O. Avci, K. Garello, M. Gabureac, et al., "Interplay of Spin-orbit Torque and Thermoelectric Effects in Ferromagnet/Normal-Metal Bilayers," *Physical Review B* 90 (2014): 224427, https://doi.org/10.1103/PhysRevB.90.224427.

46. S. Damerio and C. O. Avci, "Tunable Spin and Orbital Torques in Cu-Based Magnetic Heterostructures," *Nano Letters* 25 (2025): 2181–2187, https://doi.org/10.1021/acs.nanolett.4c05170.

47. S. Ding, P. Noël, G. K. Krishnaswamy, and P. Gambardella, "Unidirectional Orbital Magnetoresistance in Light-Metal–Ferromagnet Bilayers," *Physical Review Research* 4 (2022): L032041, https://doi.org/10.1103/PhysRevResearch.4.L032041.

48. R. Xu, X. Ning, H. Cheng, et al., "Terahertz Generation via the Inverse Orbital Rashba-Edelstein Effect at the Ni/CuO_x Interface," *Physical Review Research* 7 (2025): L012042, https://doi.org/10.1103/PhysRevResearch.7.L012042.

49. S. Krishnia, B. Bony, E. Rongione, et al., "Quantifying the Large Contribution From Orbital Rashba–Edelstein Effect to the Effective Damping-Like Torque on Magnetization," *APL Materials* 12 (2024): 051105, https://doi.org/10.1063/5.0198970.

50. K. Kondou, H. Sukegawa, S. Mitani, K. Tsukagoshi, and S. Kasai, "Evaluation of Spin Hall Angle and Spin Diffusion Length by Using Spin Current-Induced Ferromagnetic Resonance," *Applied Physics Express* 5 (2012): 073002, https://doi.org/10.1143/APEX.5.073002.

51. W. Zhang, V. Vlaminck, J. E. Pearson, R. Divan, S. D. Bader, and A. Hoffmann, "Determination of the Pt Spin Diffusion Length by Spin-Pumping and Spin Hall Effect," *Applied Physics Letters* 103 (2013): 242414, https://doi.org/10.1063/1.4848102.

52. Y. Wang, P. Deorani, X. Qiu, J. H. Kwon, and H. Yang, "Determination of Intrinsic Spin Hall Angle in Pt," *Applied Physics Letters* 105 (2014): 152412, https://doi.org/10.1063/1.4898593.

53. S. Ding, M. G. Kang, W. Legrand, and P. Gambardella, "Orbital Torque in Rare-Earth Transition-Metal Ferrimagnets," *Physical Review Letters* 132 (2024): 236702, https://doi.org/10.1103/PhysRevLett.132.236702.

54. B. Bony, S. Krishnia, Y. Xu, et al., "Quantitative Analysis of Vectorial Torques in a Thin Co 3d Ferromagnet Using Orbital-Spin Conversion," *Physical Review Applied* 23 (2025): 054038, https://doi.org/10.1103/PhysRevApplied.23.054038.

55. L. Liu, O. J. Lee, T. J. Gudmundsen, D. C. Ralph, and R. A. Buhrman, "Current-Induced Switching of Perpendicularly Magnetized Magnetic Layers Using Spin Torque From the Spin Hall Effect," *Physical Review Letters* 109 (2012): 096602, https://doi.org/10.1103/PhysRevLett.109.096602.

56. S. Shi, S. Liang, Z. Zhu, et al., "All-Electric Magnetization Switching and Dzyaloshinskii–Moriya Interaction in WTe_2/Ferromagnet Heterostructures," *Nature Nanotechnology* 14 (2019): 945–949, https://doi.org/10.1038/s41565-019-0525-8.

Supporting Information

Additional supporting information can be found online in the Supporting Information section.

Supporting File: adma73522-sup-0001-SuppMat.docx.